pharmaceutics

MDPI

Article

Fe/^{57}Fe-Metallacarboranes with Radiosensitizing Potential in Breast Cancer Cell Models: Comparative Study Between High- (^{60}Co) and Low-Energy (^{57}Co) Gamma Radiation Sources

Salvatore Di Maria [1,2], Diogo M. Engrácia [1], Catarina I. G. Pinto [1], João C. Waerenborgh [2,3,4], Bruno J. C. Vieira [1,2,3,4,*], Pedro Santos [1,2], Teresa Pinheiro [2,5], Miquel Nuez-Martínez [6], António P. Matos [7], Filipa Mendes [1,2], Francesc Teixidor [6], Clara Viñas [6] and Fernanda Marques [1,2,*]

1 Centro de Ciências e Tecnologias Nucleares (C2TN), Instituto Superior Técnico, Universidade de Lisboa, Estrada Nacional 10, Bobadela, 2695-066 Loures, Portugal; salvatore@ctn.tecnico.ulisboa.pt (S.D.M.); diogo.engracia@ctn.tecnico.ulisboa.pt (D.M.E.); catarina.pinto@ctn.tecnico.ulisboa.pt (C.I.G.P.); psantos@ctn.tecnico.ulisboa.pt (P.S.); fmendes@ctn.tecnico.ulisboa.pt (F.M.)

2 Departamento de Engenharia e Ciências Nucleares (DECN), Instituto Superior Técnico, Universidade de Lisboa, Estrada Nacional 10, Bobadela, 2695-066 Loures, Portugal; jcarlos@ctn.tecnico.ulisboa.pt (J.C.W.); murmur@ctn.tecnico.ulisboa.pt (T.P.)

3 Centro de Física e Engenharia de Materiais Avançados (CeFEMA), Instituto Superior Técnico, Universidade de Lisboa, Av. Rovisco Pais 1, 1049-001 Lisbon, Portugal

4 Laboratory of Physics for Materials and Emergent Technologies (LaPMET), Av. Rovisco Pais 1, 1049-001 Lisbon, Portugal

5 Instituto de Bioengenharia e Biociências (iBB), Instituto Superior Técnico, Universidade de Lisboa, Av. Rovisco Pais 1, 1049-001 Lisboa, Portugal

6 Institut de Ciència de Materials de Barcelona (ICMAB-CSIC), Campus U.A.B., Bellaterra, 08193 Barcelona, Spain; teixidor@icmab.es (F.T.); clara@icmab.es (C.V.)

7 Centro de Investigação Interdisciplinar Egas Moniz, Campus Universitário, Quinta da Granja, Monte de Caparica, 2829-511 Caparica, Portugal; apamatos@gmail.com

* Correspondence: brunovieira@ctn.tecnico.ulisboa.pt (B.J.C.V.); fmarujo@ctn.tecnico.ulisboa.pt (F.M.); Tel.: +351-(21)-9946260 (B.J.C.V.)

Abstract

Background: Radiosensitizers can be used to enhance tumor response and mitigate toxicity in healthy tissues during radiation therapy. This study investigates the radiosensitizing potential of the metallacarborane Fe/^{57}Fe-ferrabisdicarbollide in SK-BR-3 and MDA-MB-231 breast cancer cells, using two distinct gamma-photon sources: high-dose ^{60}Co (2.08 Gy) and low-dose ^{57}Co (37.55 mGy, ^{57}Fe Mössbauer effect). **Methods:** We evaluated cell viability and survival in 2D monolayer and 3D spheroid cultures, as well as the mechanism of cell death (ROS production, apoptosis or necrosis). Computational dosimetry was used to calculate the average absorbed dose. **Results:** In 2D models, both radiation sources induced reduced viability and increased ROS, with distinct cell death patterns dependent on the source (apoptosis or necrosis). Comparing 2D and 3D MDA-MB-231 models revealed that spheroid survival was significantly more impaired. The low-dose ^{57}Co source caused a significant radiosensitization in MDA-MB-231 spheroids, dramatically impacting viability and survival. This effect is attributed to the Mössbauer effect, where the resonant absorption of 14.41 keV radiation by ^{57}Fe leads to a massive, localized dose enhancement. The subsequent cascade of Auger and conversion electrons (local high LET) caused significantly greater cellular damage than sparse photon radiation. **Conclusions:** Fe/^{57}Fe-ferrabisdicarbollide demonstrates a potent radiosensitizing effect depending on the cell model and the radiation source used. Crucially, the observed radiosensitization allows for the development of a new, more efficient cancer radiotherapy approach that can achieve therapeutic efficacy using a significantly lower radiation dose to the patient. This paves the way for safer and better-tolerated cancer treatments.

Academic Editor: Ignacio E. León

Received: 17 December 2025
Revised: 23 January 2026
Accepted: 4 February 2026
Published: 9 February 2026

Keywords: boron clusters; ferrabisdicarbollide; radiation therapy; multimodal approaches; radiosensitizers; Mössbauer effect; breast cancer; spheroids

1. Introduction

Cancer is among the leading causes of death globally. Different options are available to treat and manage cancer, and the success of treatment depends on the type of cancer, its location, and its stage of progression. Surgery, chemotherapy and radiation therapy (external or radionuclide therapy) are the conventional treatment options aiming to improve survival rates and reduce side effects. Nevertheless, there are still challenges and limitations that need to be overcome [1–3].

External beam radiotherapy is one of the most common cancer treatments, and it is quite effective for loco-regional solid tumors [4]. Photons, in particular high-energy X-rays, are the most commonly used radiation type for external radiotherapy. However, many tumors are insensitive to radiation due to tumor type and heterogeneity, as well as resistance (either intrinsic or that acquired shortly after treatment) [5]. Moreover, despite technological advances that allow for a higher degree of tumor control, the surrounding healthy tissues are still affected [6,7].

The goal for an effective radiotherapy consists in maximizing cancer cell killing while sparing adjacent healthy tissues as much as possible. As cancer is a heterogeneous disease, great efforts have been devoted to identifying biomarkers associated with intrinsic and acquired radioresistance. Therefore, several strategies have been explored to develop radiosensitizers to enhance the radiation damage to the tumor and reduce side effects in healthy tissues, allowing radiotherapy to evolve to a more effective treatment modality [8–11].

The physical phenomenon known as the "Mössbauer effect" (Mössbauer resonant absorption), has been used as a powerful research tool in many areas of research [12] including biomedicine [13,14]. The use of the secondary radiation emitted by a ^{57}Fe nucleus excited by a ^{57}Co source was already considered a viable option for cancer treatment (Randell L. Mills, US48154476) but it remains unexplored as a targeted radiation modality. In relation to cancer therapy, very few studies have been reported since the pioneering work of R. L. Mills et al. more than 40 years ago [15]. The authors reported the elegant concept of this type of radiation in HTB26 and MCF-7 breast cancer cells after the administration of ^{57}Fe(III) bleomycin. Irradiation with resonant Mössbauer gamma-rays (14.41 keV) induced cell death, presumably by Auger cascade and secondary radiation, with extremely small radiation doses (~10^{-5} Gy), which are about 10^5 times lower than those necessary to achieve a similar effect with conventional gamma rays. This form of radiotherapy represents a method of increasing the radiosensitivity of tumors through selective energy deposition in cancer cells. A previous study revealed that the Mössbauer effect, when combined with ^{57}Fe-enriched boron clusters, could be a promising radiation modality for glioblastoma treatment [16].

Modern radiotherapy relies on accurate dosimetry to optimize cancer treatment and to avoid severe radiotoxicity [17]. Radiation dosimetry in external radiation therapy is routinely performed in clinical settings through accurate tumor treatment planning. Differential and cumulative dose–volume histograms (DVHs) are commonly used to summarize and characterize 3D dose distributions. The DVH summarizes the minimum, maximum, and median doses, as well as the dispersion near the median dose [18].

It is largely accepted that the establishment of the absorbed dose–effect relationship is of paramount importance to better plan the treatment and therefore to be able to maximize

the killing effect on tumor cells [19,20]. In addition, with the use of radiosensitizers, new challenges in terms of radiation dosimetry could be addressed. In this context, it is important to distinguish between dose enhancements, which increase the energy deposited in the target volume due to the presence of radiosensitizers, and radiosensitization, which is the increase in the biological effects of radiation using radiosensitizers. Radiosensitization is often significantly greater than the increase in physical dose, and effects are observed, for example, using clinical megavoltage X-ray sources, where the addition of a radiosensitizer leads to only negligible increases in the macroscopic dose. These results indicate that macroscopic dose enhancement alone is not a useful predictor of radiosensitization [21]. The enhanced biological outcomes observed with radiosensitizers may be partially explained by the physical dose distribution at the micro- and nanoscales, alongside with their chemical and biological effects within the target tissues.

In radiation treatment, iron complexes have not been extensively explored in combination with ionizing radiation. Only a few studies report the radiosensitizing properties of ferrocene, a benchmark sandwich organometallic complex, displaying anticancer properties [10,22,23]. The development of multifunctional small molecules with additive therapeutic effects, aimed at enhancing safety, is both a pressing need and a significant challenge in cancer treatment. Ferrabisdicarbollide ($[3,3'\text{-Fe}(1,2\text{-}C_2B_9H_{11})_2]^-$), herein abbreviated as [*o*-FESAN]$^-$, was shown to be a promising candidate for therapeutic applications as a radiosensitizer, given its exceptional chemical and thermal stability, aqueous solubility, and its ability to intercalate with double-stranded DNA [24,25].

At almost every stage of breast cancer, radiation therapy can be used and constitutes an effective method to reduce the risk of recurrence. As a result, there has been growing interest in developing new radiation protocols that minimize the dose to surrounding healthy tissues and reduce side effects. The present study investigates the radiosensitizing mechanisms and biological impacts of two different sources of gamma radiation, gamma rays (2.08 Gy) and the ^{57}Fe Mössbauer effect (37.55 mGy). The mechanisms of cell death were studied in two breast cancer cell models, SK-BR-3 and MDA-MB-231, grown in 2D monolayers or 3D spheroids (only MDA-MB-231), upon incubation with ferrabisdicarbollide ([*o*-FESAN]$^-$/[*o*-^{57}FESAN]$^-$). Cell death mechanisms were evaluated in terms of ROS production, caspase 3/7 activation and electron microscopy (TEM and SEM). Dosimetric calculations at the cellular scale are also presented.

2. Materials and Methods

2.1. Gamma Ray Irradiation Experiments

For the irradiation studies, SK-BR-3 (ATCC, HTB-30) and MDA-MB-231 (ATCC, HTB-26) cells (1–2 $\times$ 10^4 cells/well for 2D cultures, 1250 cells/well for 3D cultures) were seeded into 96-well plates and incubated with Na[*o*-FESAN] at selected concentrations for 24 h before irradiation. Irradiations were performed in the ^{60}Co experimental irradiator (PRECISA22, Pantatron Ltd., London, UK; Graviner Mfg. Co. Ltd., Gosport, UK) at C^{2}TN. Cell plates were put on a holder that rotates during the irradiation to obtain an optimized absorbed dose uniformity. The distance to the sources was set to an average dose rate of 1.01 $\pm$ 0.05 Gy min^{-1} across the whole plate. This value was obtained from a dosimetric study carried out with an FC65P ionizing chamber (IBA Dosimetry GmbH, Schwarzenbruck, Germany). Individual dose rate values were collected for each well position with the rotation system. Whenever necessary, the distance of the plates to the radioactive sources was decreased using a fine adjustment knob to compensate for the radiation decay and to maintain a constant the average dose rate.

2.2. Mössbauer Effect Absorption Irradiation Experiments

For the irradiation studies, SK-BR-3 and MDA-MB-231 cells (1–2 × 10^4 cells/well for 2D cultures, 1250 cells/well for 3D cultures) were seeded into 96-well plates and incubated with Na[*o*-^{57}FESAN] or Na[*o*-FESAN] at selected concentrations for 24 h before irradiation with 14.41 keV gamma rays for Mössbauer effect absorption. The irradiation was performed at room temperature with the ^{57}Co source (3.51 mCi/0.13 GBq), and the velocity range of the spectrometer transducer was restricted to the Doppler velocities where resonant gamma ray absorption was observed in the Mössbauer spectra of the cells [16]. This procedure implies that the sample was permanently subjected to the gamma ray appropriated for the Mössbauer effect during the irradiation time (~2 h).

2.3. Cell Line Selection, Culture Protocols, and FESAN Stock Preparation

The SK-BR-3 (ER−, PR−, HER2+) and MDA-MB-231 (triple negative, ER, PR−, HER2−) human breast cells were sourced from ATCC (Manassas, VA, USA). Growth was supported by Dulbecco's Modified Eagle's Medium (DMEM + GlutaMAX™ high glucose, Gibco™, Thermo Fisher Scientific™, Waltham, MA, USA) containing 10% fetal bovine serum (FBS), with cultures equilibrated at 37 °C in a standard moisture-saturated incubator (5% CO_2). Fresh 10 mM stock solutions of Na[*o*-FESAN] were solubilized in serum-free DMEM immediately prior to use. Subsequent working concentrations were achieved by diluting the concentrate into growth medium enriched with 10% FBS. The cytotoxic effects of the Na[*o*-FESAN] and Na[*o*-^{57}FESAN] were assessed using the MTT assay as previously reported [16]. Both compounds were solubilized in the medium to prepare serial dilutions in the range of 1–300 μM. The IC_{50} values were determined from dose–response curves using the GraphPad Prism software (version 6). For the experiments in 3D models, MDA-MB-231 spheroids were prepared in Nunclon™ Sphera™ ultra-low attachment 96U-well plates (Thermo Fischer Scientific™, Waltham, MA, USA). Briefly, cells from 80–90% confluent monolayer cultures were trypsinized and seeded at 1250 cells/well. The plate was then centrifuged at 1500 rpm for 5 min and incubated at 37 °C in a humidified atmosphere of 5% CO_2. Spheroid growth was monitored daily in a Primovert Inverted ZEISS Microscope (objective 4×, Oberkochen, Germany) with an integrated HD-cam camera, and the images were analyzed using SpheroidSizer, software version 1.0, a high-throughput MATLAB-based image analysis method (https://www.jove.com/t/51639/high-throughput-image-analysis-tumor-spheroids-user-friendly-software), accessed on 1 January 2025. The biological assays were performed when the spheroids reached diameters in the range of 350 μm (typically at day 3).

2.4. Cellular Uptake by PIXE

Cellular uptake experiments were carried out using SK-BR-3 and MDA-MB-231 cells, which were incubated with either Na[*o*-FESAN] or Na[*o*-^{57}FESAN] at a concentration of 50 μM for 24h. Untreated cells were used as controls. Cell pellets (containing ~10^6 cells/2 mL) from both cell lines were used to determine the total concentration of Fe and ^{57}Fe via the PIXE (particle-induced X-ray emission) technique after acid digestion in HNO_3, using Yttrium (CERTIPUR, Merck KGaA, Darmstadt, Germany) as an internal standard, as previously described [16]. Concentrations were expressed in ng Fe/10^6 cells. Uptake in individual MDA-MB-231 cells was also evaluated using nuclear microscopy techniques at the nuclear microprobe (Oxford Microbeams Ltd., Oxfordshire, United Kingdom) setup of the CTN/IST Van de Graaff accelerator (High Voltage Engineering, Amersfoort, The Netherlands). A 2 MeV proton beam focused to micrometer dimensions was used to image Fe distribution and visualize its preferential localization in cells. The setup and methodology are described in detail elsewhere [26].

2.5. Post-Irradiation Viability and Survival Evaluation

To assess viability, measurements were conducted 72 h post-irradiation directly within the 96-well plates. For 2D monolayers, the MTT colorimetric method was employed, while 3D cultures were analyzed via a CellTiter- Glo® 3D luminescent assay (Promega, Madison, WI, USA). Survival assessments were initiated immediately following radiation exposure. In brief, the cells or spheroids were trypsinized from the 96-well plates and the number of cells counted. Cell suspensions were then seeded in 6-well plates (3 wells per condition). The number of cells was in the range 100–300, dependent on the cell line and concentration of Na[*o*-FESAN] or Na[*o*-^{57}FESAN] used, i.e., for MDA-MB-231, 100 cells for control (no treatment), the lowest and intermediate concentrations and 200 cells for the highest, and, for SK-BR-3, 200 cells for control (no treatment), the lowest and intermediate concentrations and 300 cells for the highest concentration. Following an 11-day incubation period at 37 °C, the cultures were processed in accordance with the aforementioned protocols [16,27].

2.6. Intracellular ROS Levels

The levels of intracellular ROS were detected via fluorescence using the cell permeable probe 2′,7′-dichlorodihydrofluorescein diacetate (H_2DCF-DA) (Invitrogen, Thermo Fisher Scientific, Waltham, MA, USA). The intensity of the resulting dichlorofluorescein (DCF) fluorescence is directly proportional to the amount of ROS present in the cell [28]. For the assays, cells (~10^4 cells/well) in 96-well plates (4 wells per condition) were treated with Na[*o*-FESAN] or Na[*o*-^{57}FESAN] at 50 and 100 μM for 24 h with or without subsequent irradiation. Then, the probe (10 μM) in colorless medium (FluoroBrite™ DMEM, Gibco™, Thermo Fisher Scientific™, Waltham, MA, USA) was incubated with the cells for an additional 30 min. at 37 °C. Afterwards, the medium was removed and replaced with a fresh one. DCF fluorescence (excitation/emission: 492/517 nm) was measured throughout for 48 h utilizing a Varioskan LUX scanning multimode reader (Thermo Fisher Scientific, Waltham, MA, USA). The resulting fluorescence data (mean ± S.D.) are presented as the fold increase compared to the non-irradiated control group.

2.7. Apoptosis (Caspase-3/7 Assay)

The activity of caspase-3/7 was assessed using the Caspase-Glo® 3/7 assay kit (Promega, Madison, WI, USA). The assay uses a proluminescent substrate (DEVD-aminoluciferin) that is cleaved by active caspases-3 and -7 in apoptotic cells, which releases aminoluciferin. The free aminoluciferin reacts with luciferase in the reagent, producing a luminescent signal. The intensity of the light is directly proportional to the amount of caspase activity present in the cells.

For the assays, cells (~10^4 cells/well) in 96-well plates (four wells per condition) were treated with Na[*o*-FESAN] or Na[*o*-^{57}FESAN] at 20, 50 and 100 μM for 24 h with or without subsequent irradiation. Afterwards, 100 μL of the medium was removed from each well. Caspase 3/7® reagent was added in a 1:1 ratio, and the plate was shaken for 30 s at 300–500 rpm and then incubated at RT for 1.5 h, protected from light. The luminescent signal was measured using a Varioskan LUX scanning multimode reader (Thermo Fisher Scientific, Waltham, MA, USA). Results of luminescence (mean ± SD) were expressed as the fold change relative to non-irradiated controls.

2.8. Morphological Assessment Using TEM

MDA-MB-231 cells in the medium were seeded into 6-well plates at around 70% confluence and left to adhere overnight. Then, cells were treated with Na[*o*-FESAN] or Na[*o*-^{57}FESAN] at 50 μM for 24 h. Following the incubation period, cell cultures were subjected to irradiation using either a ^{60}Co or a ^{57}Co source. Subsequent processing was

carried out in accordance with a previously described method [16]. The fixation procedure took place after 2 h irradiation for the two irradiation modalities.

2.9. Morphological Features by SEM

MDA-MB-231 cells in the medium were seeded over glass lamellae in 6-well plates at around 70% confluence and left to adhere overnight. Then, cells were treated with Na[*o*-FESAN] or Na[*o*-^{57}FESAN] at 50 µM for 24 h. Upon incubation, cells were irradiated with the ^{60}Co source or the ^{57}Co source and processed following a previously described procedure [29]. After irradiation, the medium was discarded and the cell-covered glass lamellae were fixed in 2 mL of 3% glutaraldehyde in 0.1 M sodium cacodylate buffer, pH 7.3 for 4 h at 4 °C and rinsed three times in the same buffer. The lamellae were then dehydrated in ascending ethanol concentrations and treated three times with tert-butanol. After cooling at 4 °C, the solid samples were transferred to a vacuum desiccator containing a cooled metal block to prevent the liquefaction of the cold tert-butanol. The desiccator was evacuated using a rotary vacuum pump for two hours to allow complete sublimation of the solid tert-butanol. The freeze-dried samples were coated with gold in a JEE-4× vacuum evaporator, observed and photographed using a JEOL 5400 scanning electron microscope (JEOL USA, Peabody, MA, USA).

All remaining experimental details are available in the Supplementary Information.

3. Results and Discussion

Characterized by significant heterogeneity, breast cancer is categorized into subtypes according to the expression of estrogen (ER), progesterone (PR), and human epidermal growth factor 2 (HER2) receptors. These molecular signatures dictate specific risk assessments and therapeutic strategies [30,31]. In this study, two human breast cancer cell lines were used: SK-BR-3, which is ER- and PR- negative but exhibits HER2 overexpression, and MDA-MB-231, which serves as a model for a highly aggressive triple-negative breast cancer (TNBC) that lacks ER, PR and HER2 receptors.

Key criteria for effective radiosensitizers involve ensuring low basal cytotoxicity while maximizing the preferential uptake by neoplastic cells. The cytotoxicity of Na[*o*-FESAN] and Na[*o*-^{57}FESAN] in the two breast cancer cell lines was evaluated to select the concentrations for the cellular uptake and irradiation studies.

The IC_{50} was calculated for both compounds upon 24 h treatment, revealing that both Na[*o*-FESAN] and Na[*o*-^{57}FESAN] had similar values of IC_{50} in both cell cultures of ca. 80 µM and 100 µM for the SK-BR-3 and the MDA-MB-231 cells, respectively (Table S1), which indicates that the cytotoxicity levels of both Na[*o*-FESAN] and Na[*o*-^{57}FESAN] are similar.

3.1. Cellular Uptake Analysis

The quantification of the internalization and cellular trafficking of Na[*o*-FESAN] or Na[*o*-^{57}FESAN] in SK-BR-3 and MDA-MB-231 cell lines plays pivotal roles in the effectiveness of the effect upon irradiation. This evaluation was assessed using PIXE (Particle-Induced X-ray Emission). After incubation with the compounds at 50 µM for 24 h, the number of total Fe isotopes in cellular extracts was measured (Figure 1). We detected a relevant uptake of both Na[*o*-FESAN] and Na[*o*-^{57}FESAN], showing a 4- to 5-fold increase, depending on the cell line. This uptake reveals a significant difference in iron concentrations relative to non-treated cells (control). No major differences between the two cell lines were observed.

Visualizing the distribution of Fe in individual MDA-MB-231 cells provides direct evidence of intracellular Na[*o*-FESAN] uptake. Higher accumulation of Fe towards the

cell center (likely the nucleus) was observed in contrast to untreated controls that showed lower amounts of Fe with uniform distribution (Figure 1). These results not only provided a quantitative measure of the compound internalized by the cells but also offered insights into its subcellular localization.

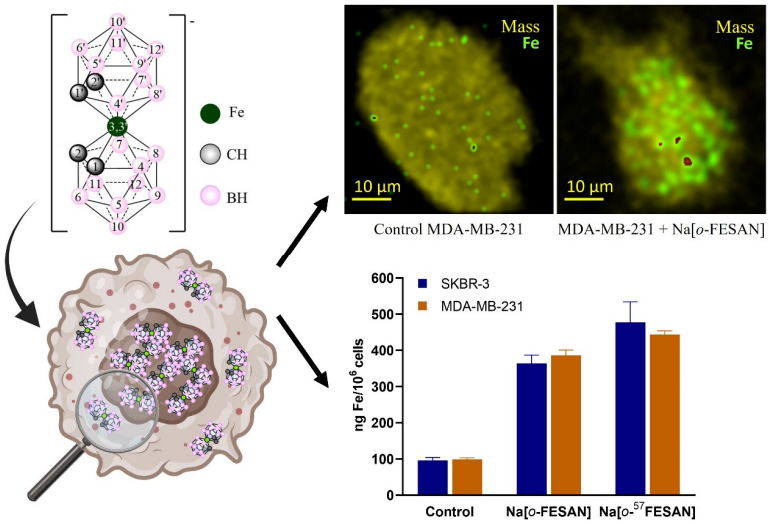

Figure 1. Schematic representation of [*o*-FESAN]$^-$, its distribution in MDA-MB-231 breast cancer cells assessed via nuclear microprobe, and uptake by PIXE in SK-BR-3 and MDA-MB-231. The nuclear microscopy images of Fe distribution (green to high intensity red) in MDA-MB-231 cells are overlapped to mass density (Mass): control and cells incubated for 24 h with 50 µM Na[*o*-FESAN] (top). The Fe content (ng Fe/10^6 cells) measured by PIXE after 24 h of exposure to Na[*o*-FESAN] at 50 µM (down).

Therefore, an increased concentration of Na[*o*-FESAN] in the nucleus can be inferred from the Fe localization in individual cells. Tagliazucchi et al. [32] proposed a theoretical model in which the translocation of particles through the nuclear pore complex depends on charge and hydrophobicity. This is consistent with the experimental results observed here, considering the known hydrophobic behavior of Na[*o*-FESAN]. Consequently, the Fe sub-cellular distribution could indicate the nucleus as a cellular target for any potential enhancement in radiosensitization.

Furthermore, melting temperature (*T*m) measurements support the existence of DNA interactions; the observed increase in the *T*m of CT-dsDNA by 4.9 ± 0.2 °C upon incubation with Na[*o*-FESAN]$^-$ is highly characteristic of an intercalative binding mode [33].

3.2. Fourier-Transform Infrared Spectroscopy (FT-IR) and Magnetic Studies of Breast Cancer Cells

The higher accumulation of Fe from [*o*-FESAN]$^-$ observed towards the center of the cell, likely in the nucleus, could raise questions about whether it remained stable during transport across membranes and whether the oxidation state of Fe^{3+} was preserved throughout this process. For this purpose, FT-IR and magnetic studies were performed in MDA-MB-231 cells after incubation with Na[*o*-FESAN]. The IR spectrum of the dry cells (Figure S1) displays the absorption at 2570 cm^{-1}, characteristic of the B-H stretching frequency observed in the Na[*o*-FESAN] spectrum taken as a reference (dotted line in Figure S1). The paramagnetic study conducted with a SQUID magnetometer shows a magnetization of approximately 0.04 µB/g at room temperature (300 K). The susceptibility data, obtained within a 5–300 K measurement range, are consistent with the existence of a paramagnetic Fe(III) complex, indicating that the oxidation state of Na[*o*-FESAN] remained unchanged after crossing the membrane in MDA-MB-231 cells.

3.3. Gamma Irradiation and Mössbauer Resonant Absorption Studies

The cell killing efficiency and anti-proliferative effect of Na[*o*-FESAN] and Na[*o*-^{57}FESAN] were evaluated after gamma irradiation and nuclear gamma resonance (^{57}Fe Mössbauer effect), respectively, both in 2D cell cultures of SK-BR-3 and MDA-MB-231 and 3D cell cultures of MDA-MB-231 (Figures 2–4). The viability and survival (clonogenic) assays were used as the two most important endpoints of the radiobiological effects [16].

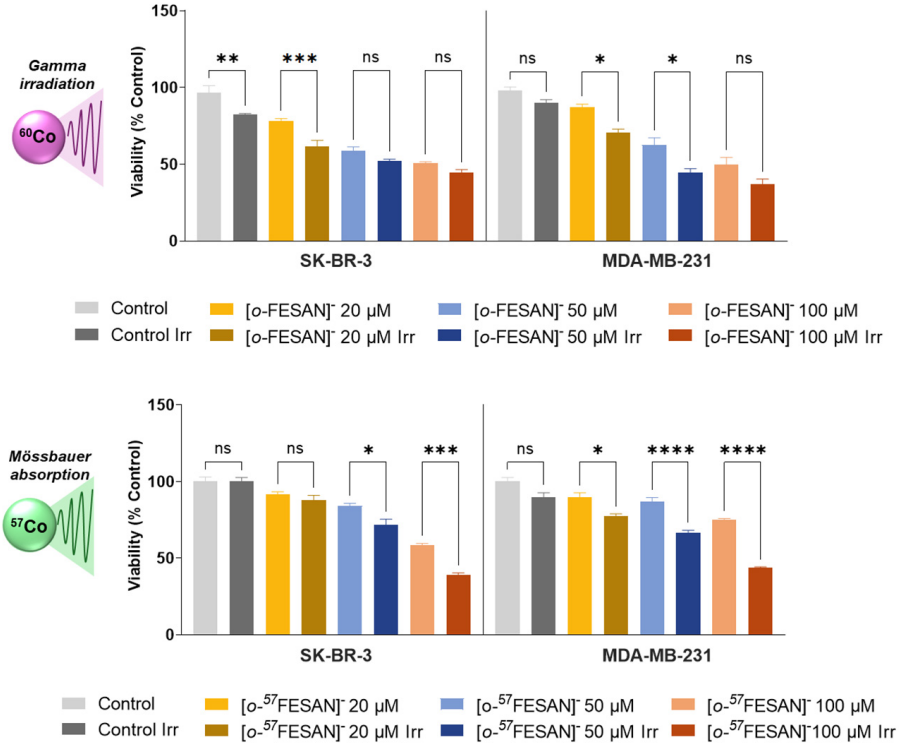

Figure 2. Cellular viability of SK-BR-3 and MDA-MB-231 cells after incubation with Na[*o*-FESAN] or Na[*o*-^{57}FESAN] at 20, 50, and 100 µM for 24 h, followed by ^{60}Co irradiation (2.08 Gy) (**top**) and ^{57}Co irradiation that induces the ^{57}Fe Mössbauer effect absorption (37.55 mGy) (**bottom**). Data are represented by the mean values ± S.E.M. of 2 to 3 independent assays, as a percentage of the control condition (cells incubated with regular culture medium and not irradiated). Statistical analysis was performed using the GraphPad Prism software. * $p < 0.05$, ** $p < 0.01$, *** $p < 0.001$, **** $p < 0.0001$; ns = non-significant.

Cells were treated for 24 h with Na[*o*-FESAN] or Na[*o*-^{57}FESAN] at concentrations of 20 µM, 50 µM, and 100 µM and irradiated with a ^{60}Co source (2.08 Gy) or with ^{57}Co radiation (37.55 mGy) suited for the ^{57}Fe Mössbauer effect experiments, respectively. The cellular viability was evaluated 72 h after irradiation. The results are shown in Figure 2, using the conventional 2D monolayer culture models.

With ^{60}Co irradiation, the decrease in cellular viability is concentration dependent and does not vary much between the two breast cancer cell lines (Figure 2, top). In addition, the difference between non-irradiated and irradiated treated cells shows low statistical significance in almost all cases apart from 20 µM in SK-BR-3 cells, where a significant radiosensitizing effect was observed. With ^{57}Co irradiation and Mössbauer effect absorption, statistically significant differences were observed in the viability of MDA-MB-231 after incubation with Na[*o*-^{57}FESAN] and irradiation at concentrations of 50 µM and higher, which indicates a radiosensitizing effect. For the SK-BR-3 cells, this effect was observed to be concentration dependent, particularly at 100 µM of Na[*o*-^{57}FESAN] (Figure 2, bottom).

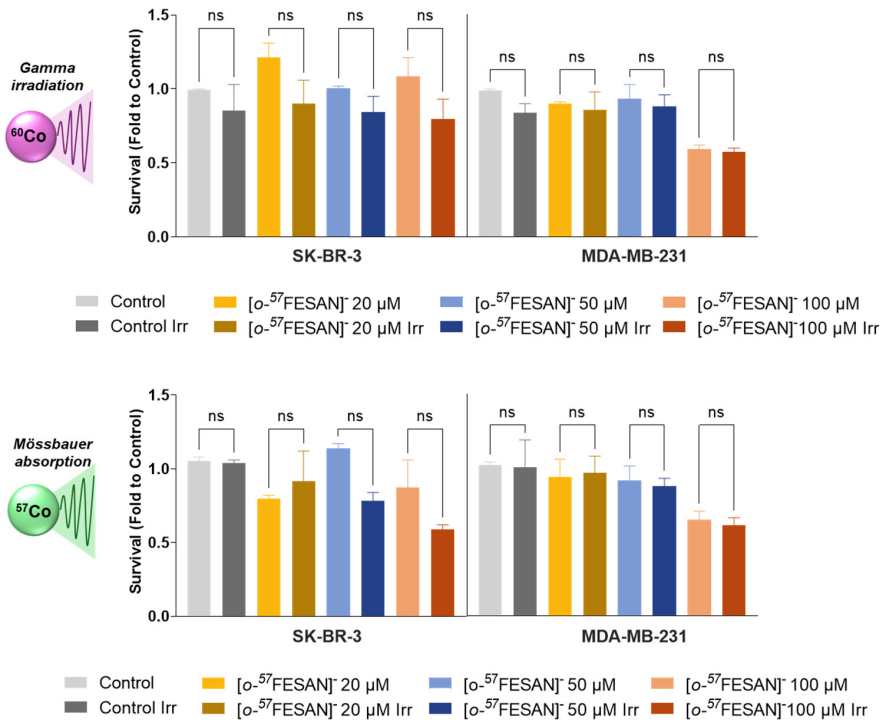

Figure 3. Cellular survival of SK-BR-3 and MDA-MB-231 cells after incubation with Na[*o*-FESAN] or Na[*o*-^{57}FESAN] at 20, 50, and 100 µM for 24 h, followed by ^{60}Co irradiation (2.08 Gy) (**top**) and ^{57}Co irradiation that induces ^{57}Fe Mössbauer effect absorption (37.55 mGy) (**bottom**). Data are represented by mean values ± S.E.M. of 2 to 3 independent assays, as a fold to the control condition (cells incubated with regular culture medium and not irradiated). Statistical analysis was performed using the GraphPad Prism software; ns = non-significant.

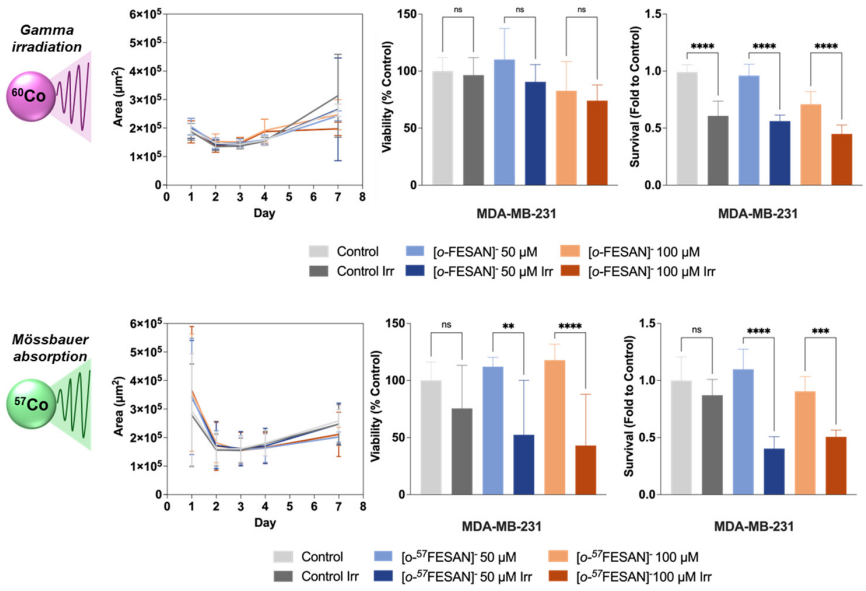

Figure 4. Effects of exposure to ^{60}Co radiation (2.08 Gy) (**top**) or to ^{57}Co source for the Mössbauer effect absorption (37.55 mGy) (**bottom**) after incubation with Na[*o*-FESAN] or Na[*o*-^{57}FESAN] at 50 and 100 µM for 24 h on the growth, cellular viability, and survival of MDA-MB-231 spheroids. Spheroids growth was represented as the mean spheroid area (mean values ± S.E.M.) as a function of time. Viability and survival data are presented as mean values ± S.E.M. of the percentage and fold to the control condition (spheroids in culture medium, non-irradiated), respectively. For all the experiments, 2 to 3 independent assays were performed. Statistical analysis was performed using the GraphPad Prism software ** $p < 0.01$, *** $p < 0.001$, **** $p < 0.0001$; ns = non-significant.

The results from the survival assays (Figure 3, top) indicate that cell survival was not affected by ^{60}Co irradiation, although an antiproliferative effect of Na[*o*-FESAN] was observed, especially for MDA-MB-231 cells incubated with 100 μM. The survival assays performed after ^{57}Co irradiation (Figure 3, bottom) demonstrate that the proliferative capacity of the breast cancer cells, in particular MDA-MB-231, was affected by Na[*o*-FESAN] in the highest concentration; however, no statistical significance was observed between the irradiated and non-irradiated conditions.

Comparing the viability results between the two types of irradiation, in both cell lines, an opposite effect is observed when increasing the concentration of Na[*o*-FESAN] or Na[*o*-^{57}FESAN]. While, in the case of ^{60}Co irradiation, a decrease in the radiosensitizing effect is observed, with ^{57}Co irradiation, the reverse was observed, i.e., there was a proportional effect between the concentration and the radiosensitizing effect. This result provides a clear indication of the superior radiosensitizing power for the combination of Na[*o*-^{57}FESAN] and ^{57}Co irradiation with Mössbauer effect absorption.

Spheroids were used as a relevant 3D cell culture model that can more accurately depict and simulate the complex environment of microtumors [16,34,35].

One important point to mention is that the proper internalization and distribution of Fe on the spheroid structure are crucial. One of the factors contributing to drug resistance is the inability of anticancer drugs to penetrate solid tumors [36,37]. In this study, ICP-MS on intact spheroids was also used to evaluate total uptake; however, it was not possible to accurately detect the presence of boron or iron on the spheroids. This probably stems from the fact that the number of cells in the spheroid sample are not sufficient to reach the detection limit of the technique.

MDA-MB-231 spheroids were incubated with Na[*o*-FESAN] or Na[*o*-^{57}FESAN] at two different concentrations, 50 and 100 μM, and irradiated with a ^{60}Co gamma source or a ^{57}Co source. The physical characterization of the spheroids upon incubation with the compounds, namely, the evaluation of the spheroids' mean area, was performed daily up to seven days. The spheroids' area, cellular viability, survival after incubation with Na[*o*-FESAN] or Na[*o*-^{57}FESAN] and exposure to the two radiations sources are shown in Figure 4 and Figure S2. The shape and overall integrity of the MDA-MB 231 spheroids did not seem to be significantly affected after irradiation.

For ^{60}Co irradiation, the loss of viability in the spheroids was less pronounced, when compared to the monolayer cultures, due to their higher sensitivity to anticancer drugs [35]. In terms of survival, a significant difference between the non-irradiated and irradiated spheroids is observed in all conditions including the control cells, demonstrating the impact of ^{60}Co radiation in the spheroid proliferative capabilities. Moreover, spheroids appear to be more sensitive to gamma rays than the 2D models. As far as we are aware, spheroids' increased sensitivity to radiation has not been reported in the literature. Further investigation may be required to elucidate whether this phenomenon is only specific to the conditions of this study [38].

After exposure to ^{57}Co radiation capable of inducing Mössbauer effect absorption, statistically significant differences in the viability of spheroids were only observed between irradiated and non-irradiated samples when incubated with Na[*o*-^{57}FESAN]. The enhanced loss of viability of incubated spheroids when compared to controls is most likely due to the synergistic interaction of ^{57}Co radiation and the Mössbauer effect induced in Na[*o*-^{57}FESAN]. In terms of survival, the Na[*o*-^{57}FESAN] appears to affect the proliferative capacities of the spheroid-derived cells in both concentrations after irradiation. Such observations are another clear indication that the combination of Na[*o*-^{57}FESAN] with exposure to ^{57}Co radiation capable of inducing the ^{57}Fe Mössbauer effect results in a radiosensitizing effect that affects cell survival. Is it important to acknowledge that,

despite our efforts to minimize the existence of a necrotic core in the spheroid, mostly by performing assays when the spheroids reached diameters in the range of 350 µm, some pre-treatment death cannot be excluded, which might affect the evaluation of the real efficacy of our therapeutic approach. Nevertheless, if this occurs, it will manifest in all spheroids in a similar manner at the beginning of the treatment, so, by normalizing the viability and survival results to the non-treated control, the potential effect can be minimized.

As a proof of concept and to confirm that the radiosensitizing effect observed in Figure 4 was due to the synergistic interaction between Na[*o*-^{57}FESAN] and the ^{57}Co source capable of inducing Mössbauer effect absorption, MDA-MB-231 spheroids were incubated with Na[*o*-FESAN] and exposed to the ^{57}Co source under the same experimental conditions. Regarding the spheroids' cellular viability and survival after incubation with Na[*o*-FESAN], no significant differences were observed between the non-irradiated and irradiated conditions, in the presence or absence of Na[*o*-FESAN] (Figure S3). These results seem to confirm that the radiosensitizing effect observed was due to the combination of Na[*o*-^{57}FESAN] with ^{57}Co radiation, capable of inducing the Mössbauer effect absorption. It is worth noting that natural iron contains ≈2.12% of ^{57}Fe, the active isotope in Mössbauer spectroscopy. Therefore, isotopic enrichment to nearly 100% in ^{57}Fe increases the effect by over 47 times.

3.4. Mechanisms of Cell Death

Radiation therapy induces both direct and indirect effects in cells. Direct effects through radiation-induced DNA damage lead to cell damage. Indirect effects, via radiolysis of water molecules, and other organic molecules in the cell, produce free radicals and ultimately cause cell death [39]. In this study, the mechanism of cell death was evaluated according to the production of reactive oxygen species (ROS), the induction of apoptosis and the examination of cellular ultrastructure details (TEM and SEM).

3.4.1. Reactive Oxygen Species (ROS)

Ionizing radiation induces oxidative stress, resulting in the generation of ROS. The increase in ROS (H_2O_2, $OH^{\bullet}$, $O^{2\bullet-}$) to a toxic level activates cell death pathways such as apoptosis or necrosis and, additionally, can damage biomolecules such as proteins, lipids, DNA, leading to alterations in their functions, with adverse cellular effects.

To better understand the effect of radiation in combination with Na[*o*-FESAN] or Na[*o*-^{57}FESAN], an evaluation of the possible radiobiological effects and mechanisms of cell death was performed. Our results showed that ^{60}Co and ^{57}Co radiation in cells incubated with Na[*o*-FESAN] or Na[*o*-^{57}FESAN] (Figures 5 and 6) increased the relative levels of ROS compared to the non-irradiated controls over time post-irradiation (until 48 h). This effect was particularly pronounced in the MDA-MB-231 cell line. For the non-irradiated cells (without/with treatment) there was no appreciable formation of ROS. A hypothetical mechanism of the radiosensitizing effect by Fe in Na[*o*-FESAN] or Na[*o*-^{57}FESAN] could involve the formation of ROS as catalysts for the Haber–Weiss cycle and the Fenton reaction, resulting in oxidative stress and cell death [10,40].

3.4.2. Apoptosis via Caspase-3/7 Activation

Caspases are a family of cysteine proteases that play critical roles in the regulation of apoptosis. Based on their mechanism of action, caspase-3 and -7 are considered executioners of the apoptosis pathways. Ionizing radiation alone or in combination with radioenhancers generates ROS and activates caspases, resulting in apoptotic cancer cells [41].

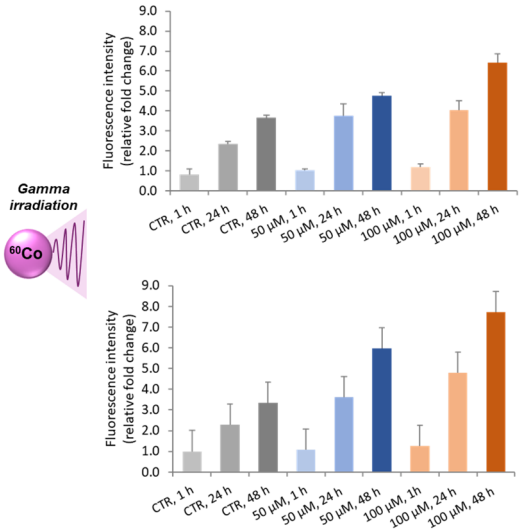

Figure 5. ROS production 1, 24 and 48 h after ^{60}Co irradiation (2.08 Gy) in SK-BR-3 (**top**) and MDA-MB-231 cells (**bottom**). Cells were treated with Na[*o*-FESAN] at 50 and 100 µM for 24 h before irradiation. Data are presented as the mean ± S.D. of two independent assays of the fold change to the control condition (non-irradiated cells incubated with regular culture medium or with Na[*o*-FESAN]).

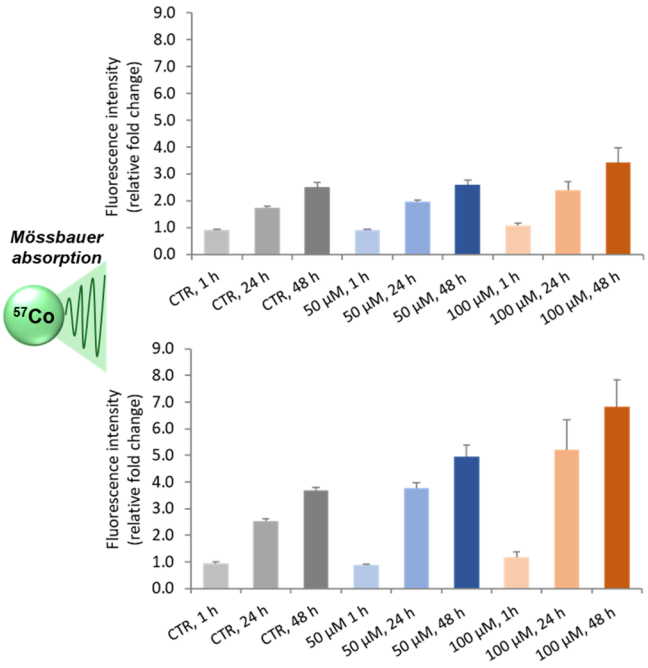

Figure 6. ROS production 1, 24 and 48 h after ^{57}Co irradiation (37.55 mGy) with Mössbauer effect absorption in SK-BR-3 (**top**) and MDA-MB-231 cells (**bottom**). Cells were treated with Na[*o*-^{57}FESAN] at 50 and 100 µM for 24 h before irradiation. Data are presented as mean ± S.D. of two independent assays of the fold change to the control condition (non-irradiated cells incubated with culture medium with Na[*o*-^{57}FESAN]).

We investigated the possible activation of apoptotic events in SK-BR-3 and MDA-MB-231 cells treated with Na[*o*-FESAN or Na[*o*-^{57}FESAN] at concentrations of 20, 50 and 100 µM for 24 h before irradiation. As shown in Figure 7, the ability of the complexes to activate caspase-3/7 is mostly dependent on the type of cells rather than the type of radiation. SK-BR-3 cells treated with Na[*o*-FESAN or Na[*o*-^{57}FESAN] exhibited lower caspase activation. Interestingly, and in particular for the Mössbauer effect absorption, caspase activation seemed to be in line with the production of ROS.

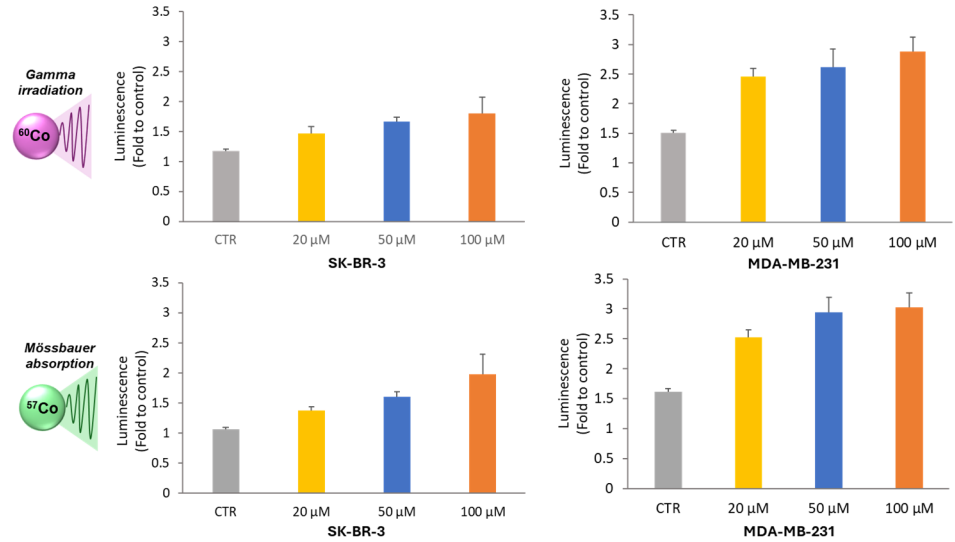

Figure 7. Caspase 3/7 activation after ^{60}Co irradiation (2.08 Gy) in SK-BR-3 and MDA-MB-231 cells (**top**) or ^{57}Co irradiation (37.55 mGy) with Mössbauer effect absorption in SK-BR-3 and MDA-MB-231 cells (**bottom**). Cells were treated with Na[*o*-FESAN] or Na[*o*-^{57}FESAN] at 20 µM, 50 µM and 100 µM for 24 h before irradiation. Data in luminescent units are expressed as the mean ± SD of two independent assays of the fold change to the control condition (non-irradiated cells incubated with culture medium or with Na[o-^{7}FESAN] or Na[o-^{57}FESAN].

3.4.3. Transmission Electron Microscopy (TEM) Studies

TEM studies of the morphological alterations in MDA-MB-231 cells, before and 2 h post-irradiation with ^{60}Co and ^{57}Co sources, are depicted in Figure 8. The results showed that, under the control conditions (without any treatment), cells had a normal morphology (Figure 8(a1)) and cells incubated with (50 µM) Na[*o*-FESAN] only displayed denser cytoplasmic matrix and vesiculation of cellular organelles, disclosing some toxicity to the cells, although cell death was not detected (Figure 8(a2)). Cells treated with Na[*o*-FESAN] (50 µM) and exposed to ^{60}Co gamma rays showed disorganization of cell architecture and signs of necrosis such as rupture of the plasma membrane (Figure 8b). Cells irradiated with a ^{57}Co source exhibiting a ^{57}Fe Mössbauer effect on Na[*o*-^{57}FESAN]-treated cells (50 µM) (Figure 8c) showed less damage compared to ^{60}Co irradiation, but many cells displayed signs of apoptosis such as blebs of the cell surface in accordance with caspase activation.

(**a**) controls (**b**) ^{60}Co-Gamma irradiation (**c**) ^{57}Co-Mössbauer effect

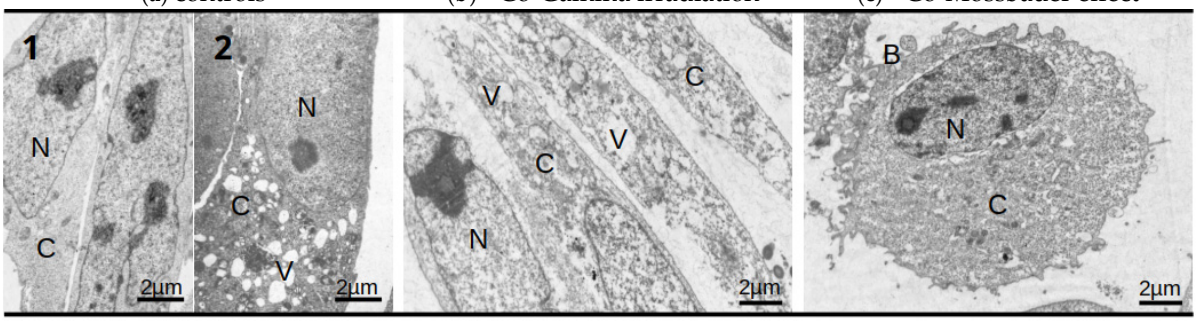

Figure 8. TEM studies comparing the morphological alterations in MDA-MB-231 cells, before treatment (control) (**a**), 2 h after irradiation with ^{60}Co (**b**) and with ^{57}Co (**c**). Controls were cells with no treatment, which had a normal morphology (**a1**) or cells incubated with Na[*o*-FESAN], which showed vesiculation of cellular organelles but no signs of cytotoxicity (**a2**). Cells treated with Na[*o*-FESAN] and gamma rays showed signs of plasma membrane rupture and necrosis (**b**). The ^{57}Co induced ^{57}Fe Mössbauer effect on Na[*o*-^{57}FESAN]-treated cells showed signs of apoptosis (**c**). N-nucleus; C-cytoplasm; V-vacuoles; B-plasma membrane blebs.

Results showed that, 2 h after irradiation, MDA-MB-231 cells showed signs of apoptosis after exposure to 37.55 mGy of ^{57}Co source and necrosis after 2.08 Gy of ^{60}Co source. Although different cell types have distinct radiation sensitivities, the pattern of cell death following radiation is generally dose dependent. While high doses are more prone to induce necrosis, low doses tend to trigger apoptosis [42]. These cell death modalities have a distinct effect on the immune system. While necrosis is linked to an inflammatory response, apoptosis is considered a less immunogenic cell death modality, suggesting that a low dose would be non-immunogenic, in contrast to a high dose [43].

3.4.4. Scanning Electron Microscopy (SEM)

Scanning electron microscopy can visualize in detail the surface of the cells, in particular the morphological features of cells undergoing apoptosis, which include membrane blebbing and loss of features, such as microvilli [44]. SEM studies were performed with untreated MDA-MB-231 cells (controls) and MDA-MB-231 cells treated with Na[*o*-FESAN] or Na[*o*-^{57}FESAN] with/without ^{60}Co or ^{57}Co source irradiation. The results in Figure 9 depicted the cells before and 2 h post-irradiation. The results showed that, in the control conditions (Figure 9a) (without any treatment), cells appeared under division (white cells) uniform in size and shape and with well-organized structures that are not so evident in Na[*o*-^{57}FESAN]-treated cells only (Figure 9b). For the ^{57}Co-irradiated control cells (Figure 9c), some lost their microvilli and the cell surface displays an irregular texture, presumably related to the irradiation treatment. In ^{60}Co-irradiated Na[*o*-FESAN]-treated cells (Figure 9d), the results showed that they lost most of their microvilli due to the disruption of cellular integrity and even showed cells destroyed by radiation damage, compatible with necrosis. In ^{57}Co-irradiated Na[*o*-^{57}FESAN]-treated cells (Figure 9e), many displayed a rounded condensed form, as well as smaller sizes and bleb aggregates in the extracellular space and over the cells, compatible with apoptosis.

3.5. Comparative Dosimetry Studies

The aim of this dosimetry study was twofold: (i) to estimate the cell-absorbed doses, because they significantly influence the relationship between absorbed dose and cell survival, which, in turn, affects models for DNA repair mechanisms, killing effects, and other related processes; [45] (ii) to estimate the potential radioenhancement (physical dose enhancement) of ^{57}Fe radiosensitizer materials on tumor cells irradiated with a Mössbauer setup (using 14.41 keV ^{57}Co resonant irradiation), and to compare this effect with ^{60}Co irradiation.

The absorbed dose per cell estimations obtained for the two-irradiation modalities are reported in Table 1. The MC model used to simulate external photon and electron irradiations, as well as the one used to simulate the lines emission of ^{57}Fe after 14.41 keV resonant absorption, is reported in Figure 10.

Table 1. Calculated cellular doses for ^{57}Co (Mössbauer effect) and ^{60}Co irradiations, irradiation time and starting activity).

Irradiation Type	Contribution Type ID	Irradiation Time Duration (s)	Average Absorbed Dose per Cell (Gy)
Mössbauer (14.41 keV with ^{57}Co decay)	C1	7200 (starting activity 0.13 GBq)	2.7×10^{-2} (7.3 keV K-conversion electrons) 7.75×10^{-3} (5.6 keV KLL Auger electrons) 2.8×10^{-3} (6.4 keV KX-ray)
Photoelectric (photons of 14.41 keV with ^{57}Co decay)	C2	7200 (starting activity 0.13 GBq)	1.4×10^{-5}
Photons of 122 keV (^{57}Co decay)	C3	7200 (starting activity 0.13 GBq)	1.3×10^{-5}

Table 1. *Cont.*

Irradiation Type	Contribution Type ID	Irradiation Time Duration (s)	Average Absorbed Dose per Cell (Gy)
Photon of 136 keV (^{57}Co decay)	C4	7200 (starting activity 0.13 GBq)	1.6×10^{-6}
Electrons of 130 keV (^{57}Co decay)	C5	7200 (starting activity 0.13 GBq)	3.6×10^{-4}
Electrons of 115 keV (^{57}Co decay)	C6	7200 (starting activity 0.13 GBq)	6.1×10^{-4}
Gamma-rays (^{60}Co decay, 1.33 MeV)	C7	120 (starting activity 52 TBq)	2.08

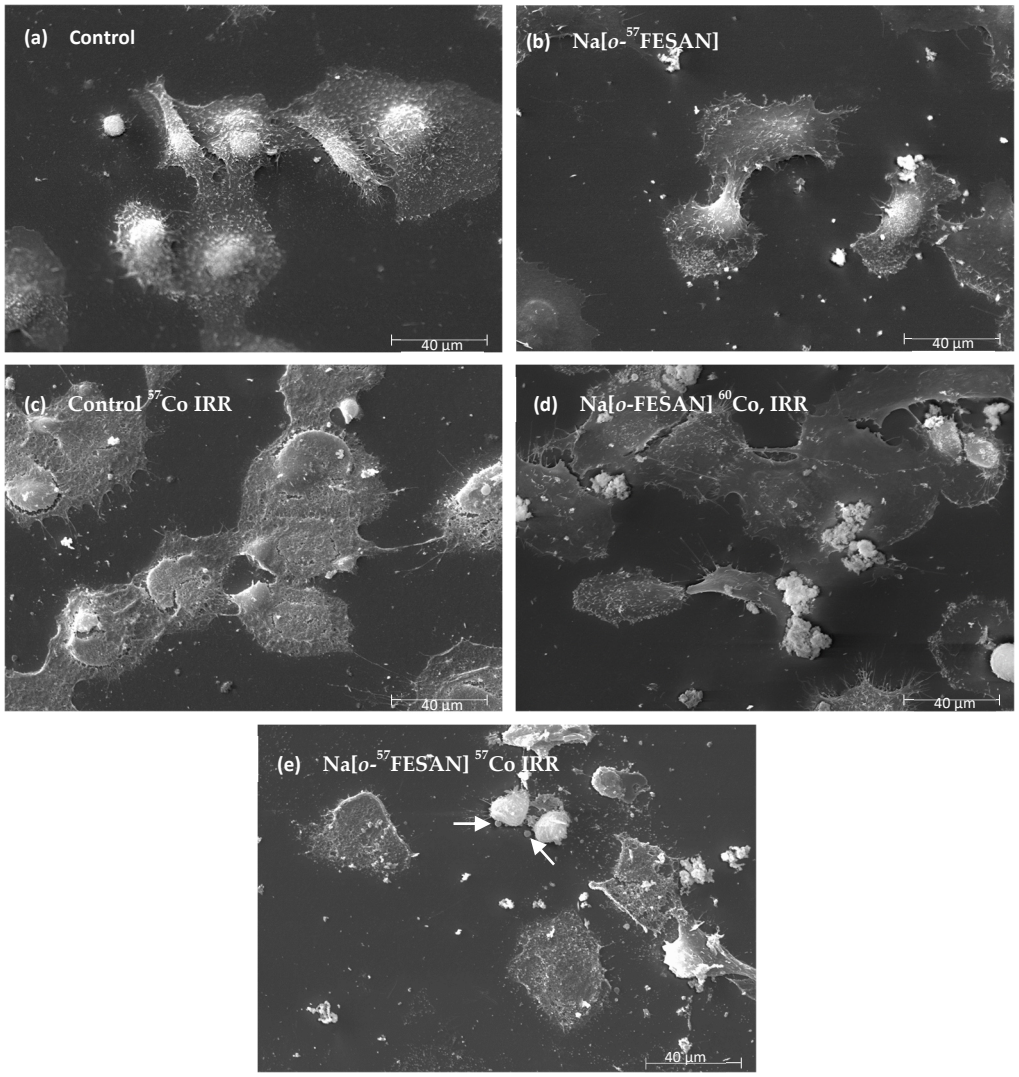

Figure 9. SEM studies comparing the morphological features in MDA-MB-231 cells, before treatment (control) (**a**), cells treated with Na[*o*-^{57}FESAN] only (**b**), untreated cells 2 h after irradiation with ^{57}Co (**c**), ^{60}Co-irradiated Na[*o*-FESAN]-treated cells (**d**) and ^{57}Co-irradiated Na[*o*-^{57}FESAN]-treated cells showing signs of apoptosis (**e**). Plasma membrane blebs are indicated by white arrows.

The estimated cell-absorbed doses in Table 1 show a strong correlation with the viability results from both the 2D cell and 3D spheroid experiments.

The results obtained in Figure S3 are an example of this correlation. They show the viability and survival of MDA-MB-231 spheroids incubated with Na[*o*-FESAN] (without considering the Mössbauer effect). This reveals no radiosensitizer effect, since, in this case, the estimated total absorbed dose per cell is only in the order of 1 mGy (sum of the contributions C2 + C3 + C4 + C5 + C6 in Table 1).

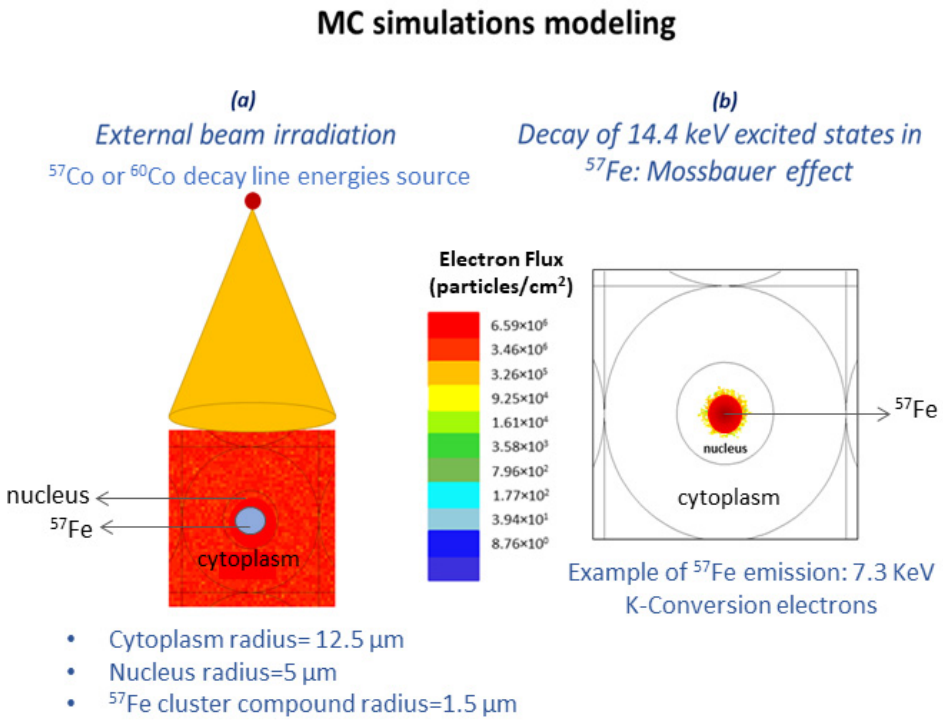

Figure 10. Monte Carlo modeling setups for external irradiation by photon or electron emission by the source decay of ^{60}Co or ^{57}Co (**a**) and example of conversion electrons simulations (**b**) emitted by ^{57}Fe after the resonant 14.41 keV photon line absorption.

Nowadays, there is a high degree of certainty that multicellular tumor spheroids, in contrast to monolayer cultures, can mimic some of the in vivo tumor features more accurately, due to similar growth behaviors as well as cellular heterogeneity within the spheroid, and the formation of molecular gradients, among others.

This is particularly evident for Mössbauer irradiation (see Figure 2 bottom). When Mössbauer is considered (contribution C1 in Table 1), it is possible to see a significative dose enhancement effect (Figure 2 bottom) of a factor of about 37 in contrast to the absence of the Mössbauer effect (Figure S3), which corresponds only to the contributions C2 + C3 + C4 + C5 + C6 of Table 1. The dose enhancement is mainly due to the large electron cascade (Auger and Conversion) and X-ray emission after the resonant absorption of 14.41 keV line by ^{57}Fe. In fact, this physical dose increase correlates well with the Mössbauer viability and survival data results and is evident in the case of 50 and 100 µM Na[*o*-^{57}FESAN], for 3D cell cultures (Figure 4) and 2D viability studies (Figure 2).

Importantly, even if the cell-absorbed doses with ^{57}Co irradiation (Mössbauer effect) are lower than those obtained for ^{60}Co gamma irradiation, the radiosensitizer effect detected should be due to the local high LET and low-energy electrons that are able to cause significant cell damage, in contrast to the sparse photon radiation distribution. It is also important to note that, even if the ^{57}Co decay involves several decay particles, as shown in Table 1 (e.g., photons of 136 keV or electrons of 130 keV), these contributions are two or three orders of magnitude lower than the Mössbauer contribution (contribution C1 in Table 1).

Ultimately, significant constraints persist in radiation dosimetry across both experimental and theoretical frameworks. Empirical measurements can be subject to uncertainties as high as 30%, stemming primarily from challenges in geometric configuration and experimental reproducibility [46]. Statistical uncertainties linked to the computational simulations were at most 5%, depending on the energy of the source particle. Low-energy electrons related to the C1 component can be measured (e.g., β spectroscopy) with energy resolutions

less than 2%. The systematic uncertainty linked to these line energies on MC input is consequently low. Major uncertainties arise from the limited availability of experimental cross-sections for low-energy electrons in liquid water, which necessitates a reliance on theoretical cross-section models. The use of different models for low-electron energy cross sections can account for a variability in dose estimation of about 20% until 1 keV and can reach even greater uncertainty for energy less than 1 keV [47,48].

4. Conclusions

In this study, we examined the radiosensitizing effects of Na[*o*-FESAN] using two different radiation sources (^{60}Co 2.08 Gy and ^{57}Co 37.55 mGy) in breast cancer cells SK-BR-3 and MDA-MB-231. The cellular uptake studies of Na[*o*-FESAN] by nuclear microscopy/PIXE (Fe) showed a four- to five-fold increase in Fe in treated cells as compared to non-treated controls. Additionally, it also observed that Fe within single cells showed a preferential accumulation in the cell center, likely the nucleus. FT-IR and magnetic studies showed that, after the uptake of Na[*o*-FESAN] by the cells, the Fe retains its electronic state as Fe^{3+}.

The potential of Na[*o*-FESAN] or Na[*o*-^{57}FESAN] as radiosensitizers for ^{60}Co radiation (2.08 Gy) and ^{57}Co radiation (37.55 mGy) able to induce the ^{57}Fe Mössbauer effect, was explored in 2D cultures of SK-BR-3 and MDA-MB-231 cells. An important loss of cellular viability was detected with both radiation sources, but no important inhibition of long-term proliferation was observed. The modes of cell death via apoptosis and/or necrosis were dependent on the type of radiation and evidence suggests they are mediated by ROS. TEM and SEM studies revealed distinct cell death mechanisms for each radiation source. Treated cells exposed to ^{60}Co radiation showed signs of necrosis, while those exposed to ^{57}Co radiation exhibited less damage and signs of apoptosis. These findings are also supported by the caspase-3/7 studies. The intercalation ability of Na[*o*-^{57}FESAN], combined with its accumulation at the center of the cell, probably the nucleus, observed via nuclear microprobe, strongly supports a mechanism where the Auger cascades are generated in the immediate vicinity of the nucleus, leading to high-LET (linear energy transfer) damage that may be the origin of the observed lethality.

This study also compared the response to radiation in 3D MDA-MB-231 cell cultures irradiated with ^{60}Co and ^{57}Co. The survival studies showed significantly higher radiosensitivity in spheroids in comparison to the 2D models. This difference in radiosensitivity is particularly significant in the case of ^{57}Co irradiation, given the low radiation dose used and the fact that tumor spheroids more closely mimic some characteristics of in vivo tumors. Moreover, the precise collimation of the 14.41 keV radiation originated in the ^{57}Co source, necessary for Mössbauer absorption, will amplify the dose–effect relationship, potentially further reducing the overall radiation exposure to patients while maintaining therapeutic efficacy.

The MC dosimetry simulations confirmed the strong local dose induced by the Mössbauer effect, validating the hypothesis of a synergistic cellular damage effect that far exceeds the dose contributed by the conventional photoelectric effect alone.

Our data suggest that ferrabisdicarbollides offer notable potential for enhancing and optimizing radiotherapy from a multimodal perspective. Because Na[*o*-^{57}FESAN] exhibits good biocompatibility (high IC_{50}), we anticipate that the concentrations required for the Mössbauer-triggered effect can be achieved through localized delivery strategies such as intratumoral injection or targeted nanoparticle formulations in combination with localized radiotherapy, such as intraoperative radiation therapy, thereby minimizing systemic exposure and confining the effects triggered by the high-LET (linear energy transfer) particles

to the tumor volume. These promising results underscore the potential for significant advancements in developing future new small-molecule radiosensitizers for cancer treatment.

Supplementary Materials: The following supporting information can be downloaded at: https://www.mdpi.com/article/10.3390/pharmaceutics18020214/s1, Figure S1: (a) FT-IR spectra of dry MDA-MB-231 cells after 6 h of incubation with Na[*o*-FESAN] at 100 μM. (b) Magnetic susceptibility of dry MDA-MB-231 cells after 6 h of exposure to Na[*o*-FESAN] at 100 μM.; Figure S2: Illustrative microscope images of the effects of exposure to ^{60}Co radiation (2.08 Gy) (top) and to ^{57}Co source suitable for Mössbauer effect absorption (37.55m mGy) (bottom) after incubation with Na[*o*-FESAN] or Na[*o*-^{57}FESAN] at 50 and 100 μM for 24 h on the growth of MDA-MB-231 spheroids.; Figure S3: Effects of exposure to ^{57}Co source (37.55 mGy) after incubation with Na[*o*-FESAN] at 50 and 100 μM for 24 h on the cellular viability, and survival of MDA-MB-231 spheroids. Viability and survival data are presented as mean values ± S.E.M. of the percentage and the fold to the control condition (spheroids incubated with regular culture medium and not irradiated), respectively. For all the experiments, 2 to 3 independent assays were performed.; Table S1: The IC_{50} values found with Na[*o*-FESAN] and Na[*o*-^{57}FESAN] for both cell lines after 24 h exposure.; Additional Materials and Experimental Details. The references in supplementary material can be found in [33,49–55].

Author Contributions: Conceptualization, F.M. (Fernanda Marques); methodology, S.D.M., D.M.E., C.I.G.P., J.C.W., B.J.C.V., P.S., T.P., M.N.-M., A.P.M., F.M. (Filipa Mendes), F.T., C.V. and F.M. (Fernanda Marques); validation, S.D.M., D.M.E., C.I.G.P., J.C.W., B.J.C.V., T.P., M.N.-M., A.P.M., F.M. (Filipa Mendes), F.T., C.V. and F.M. (Fernanda Marques); formal analysis, S.D.M., D.M.E., C.I.G.P., J.C.W., B.J.C.V., T.P., M.N.-M., A.P.M., F.M. (Filipa Mendes), F.T., C.V. and F.M. (Fernanda Marques); investigation, S.D.M., D.M.E., C.I.G.P., J.C.W., B.J.C.V., P.S., T.P., M.N.-M., A.P.M., F.M. (Filipa Mendes), F.T., C.V. and F.M. (Fernanda Marques); resources, S.D.M., J.C.W., B.J.C.V., P.S., T.P., A.P.M., F.M. (Filipa Mendes), F.T., C.V. and F.M. (Fernanda Marques); data curation, S.D.M., B.J.C.V., T.P., F.M. (Filipa Mendes), F.T., C.V. and F.M. (Fernanda Marques); writing—original draft preparation, S.D.M., D.M.E., C.I.G.P., J.C.W., B.J.C.V., T.P., A.P.M., F.M. (Filipa Mendes), F.T., C.V. and F.M. (Fernanda Marques); writing—review and editing, B.J.C.V., T.P., F.M. (Filipa Mendes), F.T., C.V. and F.M. (Fernanda Marques); visualization, S.D.M., D.M.E., C.I.G.P., J.C.W., B.J.C.V., P.S., T.P., M.N.-M., A.P.M., F.M. (Filipa Mendes), F.T., C.V. and F.M. (Fernanda Marques); supervision, B.J.C.V. and F.M. (Fernanda Marques); project administration, F.M. (Fernanda Marques); funding acquisition, S.D.M., J.C.W., B.J.C.V., P.S., T.P., F.M. (Filipa Mendes), F.T., C.V. and F.M. (Fernanda Marques). All authors have read and agreed to the published version of the manuscript.

Funding: This research was partially funded by the Spanish Ministerio de Economía y Competitividad (PID2019-106832RB-100, PID2020-116728RB-I00), the Generalitat de Catalunya (2017SGR1720), Fundação para a Ciência e Tecnologia, Portugal (FCT) through the projects UID/Multi/04349/2020 (C2TN), UIDP/04565/2020 (iBB/IST), LA/P/0140/2020 (Associate Laboratory Institute for Health and Bioeconomy—i4HB), National Infrastructure Roadmap, LTHMFL-NECL and LISBOA-01-0145-FEDER-022096. FCT also funded PhD Fellowships 2020.07119.BD to C.I.G.P. and PRT/BD/154855/2023 to D.M.E. F.M. acknowledges FCT and Campus France for PESSOA grant 2021.09137.CBM, and FCT and UTAustin Portugal Program for project 2022.15449.UTA.

Institutional Review Board Statement: Not applicable.

Informed Consent Statement: Not applicable.

Data Availability Statement: The original contributions presented in this study are included in the article and supplementary material. Further inquiries can be directed to the corresponding author.

Acknowledgments: The authors thank Moulay Sougrati, from the Charles Gerhardt Institute, ICGM UMR 5253, Montpellier, France, for the kind gift of $^{57}FeCl_2$.

Conflicts of Interest: The authors declare no conflicts of interest. The funders had no role in the design of the study; in the collection, analyses, or interpretation of data; in the writing of the manuscript; or in the decision to publish the results.

Abbreviations

The following abbreviations are used in this manuscript:

ROS	Reactive Oxygen Species
LET	Linear Energy Transfer
DVH	Dose-Volume Histogram
[*o*-FESAN]$^-$	[3,3′-Fe(1,2-$C_2B_9H_{11}$)$_2$]$^-$
[*o*-^{57}FESAN]$^-$	[3,3′-^{57}Fe(1,2-$C_2B_9H_{11}$)$_2$]$^-$
TEM	Transmission Electron Microscopy
SEM	Scanning Electron Microscopy
ATCC	American Type Culture Collection
DMEM	Dulbecco's Modified Eagle's Medium
FBS	Fetal Bovine Serum
PIXE	Particle-Induced X-ray Emission
T_m	Melting Temperature
H_2DCF-DA	2′,7′-dichlorodihydrofluorescein diacetate
DCF	2′,7′-dichlorofluorescein
ER	Estrogen
PR	Progesterone
HER2	Human Epidermal Growth Factor 2
TNBC	Triple-Negative Breast Cancer
FT-IR	Fourier-Transform Infrared Spectroscopy
ICP-MS	Inductively Coupled Plasma Mass Spectrometry
MC	Monte Carlo

References

1. Arruebo, M.; Vilaboa, N.; Sáez-Gutierrez, B.; Lambea, J.; Tres, A.; Valladares, M.; González-Fernández, Á. Assessment of the Evolution of Cancer Treatment Therapies. *Cancers* **2011**, *3*, 3279–3330. [CrossRef]
2. Bray, F.; Laversanne, M.; Sung, H.; Ferlay, J.; Siegel, R.L.; Soerjomataram, I.; Jemal, A. Global Cancer Statistics 2022: GLOBOCAN Estimates of Incidence and Mortality Worldwide for 36 Cancers in 185 Countries. *CA Cancer J. Clin.* **2024**, *74*, 229–263. [CrossRef]
3. Miller, K.D.; Nogueira, L.; Devasia, T.; Mariotto, A.B.; Yabroff, K.R.; Jemal, A.; Kramer, J.; Siegel, R.L. Cancer Treatment and Survivorship Statistics, 2022. *CA Cancer J. Clin.* **2022**, *72*, 409–436. [CrossRef]
4. Baskar, R.; Lee, K.A.; Yeo, R.; Yeoh, K.-W. Cancer and Radiation Therapy: Current Advances and Future Directions. *Int. J. Med. Sci.* **2012**, *9*, 193–199. [CrossRef] [PubMed]
5. Olivares-Urbano, M.A.; Griñán-Lisón, C.; Marchal, J.A.; Núñez, M.I. CSC Radioresistance: A Therapeutic Challenge to Improve Radiotherapy Effectiveness in Cancer. *Cells* **2020**, *9*, 1651. [CrossRef]
6. Schaue, D.; McBride, W.H. Opportunities and Challenges of Radiotherapy for Treating Cancer. *Nat. Rev. Clin. Oncol.* **2015**, *12*, 527–540. [CrossRef]
7. Chen, H.H.W.; Kuo, M.T. Improving Radiotherapy in Cancer Treatment: Promises and Challenges. *Oncotarget* **2017**, *8*, 62742–62758. [CrossRef] [PubMed]
8. Komorowska, D.; Radzik, T.; Kalenik, S.; Rodacka, A. Natural Radiosensitizers in Radiotherapy: Cancer Treatment by Combining Ionizing Radiation with Resveratrol. *Int. J. Mol. Sci.* **2022**, *23*, 10627. [CrossRef]
9. Wang, H.; Mu, X.; He, H.; Zhang, X.-D. Cancer Radiosensitizers. *Trends Pharmacol. Sci.* **2018**, *39*, 24–48. [CrossRef] [PubMed]
10. Gong, L.; Zhang, Y.; Liu, C.; Zhang, M.; Han, S. Application of Radiosensitizers in Cancer Radiotherapy. *Int. J. Nanomed.* **2021**, *16*, 1083–1102. [CrossRef]
11. Neufeld, M.J.; Lutzke, A.; Pratx, G.; Sun, C. High-*Z* Metal–Organic Frameworks for X-ray Radiation-Based Cancer Theranostics. *Chem. A Eur. J.* **2021**, *27*, 3229–3237. [CrossRef] [PubMed]
12. Sharma, V.K.; Klingelhöfer, G.; Nishida, T. (Eds.) *Mössbauer Spectroscopy*; Wiley: Hoboken, NJ, USA, 2013.
13. Kamnev, A.A.; Tugarova, A.V. Bioanalytical Applications of Mössbauer Spectroscopy. *Russ. Chem. Rev.* **2021**, *90*, 1415–1453. [CrossRef]
14. Kamnev, A.A.; Tugarova, A.V. Sample Treatment in Mössbauer Spectroscopy for Protein-Related Analyses: Nondestructive Possibilities to Look inside Metal-Containing Biosystems. *Talanta* **2017**, *174*, 819–837. [CrossRef] [PubMed]
15. Mills, R.L.; Walter, C.W.; Venkataraman, L.; Pang, K.; Farrell, J.J. A Novel Cancer Therapy Using a Mössbauer-Isotope Compound. *Nature* **1988**, *336*, 787–789. [CrossRef] [PubMed]

16. Buades, A.B.; Pereira, L.C.J.; Vieira, B.J.C.; Cerdeira, A.C.; Waerenborgh, J.C.; Pinheiro, T.; Matos, A.P.A.; Pinto, C.G.; Guerreiro, J.F.; Mendes, F.; et al. The Mössbauer Effect Using ^{57}Fe-Ferrabisdicarbollide ([*o*-^{57}FESAN]$^{-}$): A Glance into the Potential of a Low-Dose Approach for Glioblastoma Radiotherapy. *Inorg. Chem. Front.* **2022**, *9*, 1490–1503. [CrossRef]
17. Kron, T.; Lehmann, J.; Greer, P.B. Dosimetry of Ionising Radiation in Modern Radiation Oncology. *Phys. Med. Biol.* **2016**, *61*, R167–R205. [CrossRef]
18. Cheng, L.; Hobbs, R.F.; Segars, P.W.; Sgouros, G.; Frey, E.C. Improved Dose–Volume Histogram Estimates for Radiopharmaceutical Therapy by Optimizing Quantitative SPECT Reconstruction Parameters. *Phys. Med. Biol.* **2013**, *58*, 3631–3647. [CrossRef]
19. Chiesa, C.; Bardiès, M.; Zaidi, H. Voxel-based Dosimetry Is Superior to Mean Absorbed Dose Approach for Establishing Dose-effect Relationship in Targeted Radionuclide Therapy. *Med. Phys.* **2019**, *46*, 5403–5406. [CrossRef]
20. McMahon, S.J.; Paganetti, H.; Prise, K.M. Optimising Element Choice for Nanoparticle Radiosensitisers. *Nanoscale* **2016**, *8*, 581–589. [CrossRef]
21. Butterworth, K.T.; McMahon, S.J.; Currell, F.J.; Prise, K.M. Physical Basis and Biological Mechanisms of Gold Nanoparticle Radiosensitization. *Nanoscale* **2012**, *4*, 4830. [CrossRef]
22. Skoupilova, H.; Bartosik, M.; Sommerova, L.; Pinkas, J.; Vaculovic, T.; Kanicky, V.; Karban, J.; Hrstka, R. Ferrocenes as New Anticancer Drug Candidates: Determination of the Mechanism of Action. *Eur. J. Pharmacol.* **2020**, *867*, 172825. [CrossRef] [PubMed]
23. Gill, M.R.; Vallis, K.A. Transition Metal Compounds as Cancer Radiosensitizers. *Chem. Soc. Rev.* **2019**, *48*, 540–557. [CrossRef]
24. Gutiérrez-Gálvez, L.; García-Mendiola, T.; Lorenzo, E.; Nuez-Martinez, M.; Ocal, C.; Yan, S.; Teixidor, F.; Pinheiro, T.; Marques, F.; Viñas, C. Compelling DNA Intercalation through 'Anion–Anion' Anti-Coulombic Interactions: Boron Cluster Self-Vehicles as Promising Anticancer Agents. *J. Mater. Chem. B* **2024**, *12*, 9550–9565. [CrossRef]
25. Citrin, D.E. Recent Developments in Radiotherapy. *N. Engl. J. Med.* **2017**, *377*, 1065–1075. [CrossRef] [PubMed]
26. Ribeiro, N.; Roy, S.; Butenko, N.; Cavaco, I.; Pinheiro, T.; Alho, I.; Marques, F.; Avecilla, F.; Costa Pessoa, J.; Correia, I. New Cu(II) Complexes with Pyrazolyl Derived Schiff Base Ligands: Synthesis and Biological Evaluation. *J. Inorg. Biochem.* **2017**, *174*, 63–75. [CrossRef] [PubMed]
27. Nuez-Martínez, M.; Queralt-Martín, M.; Muñoz-Juan, A.; Aguilella, V.M.; Laromaine, A.; Teixidor, F.; Viñas, C.; Pinto, C.G.; Pinheiro, T.; Guerreiro, J.F.; et al. Boron Clusters (Ferrabisdicarbollides) Shaping the Future as Radiosensitizers for Multimodal (Chemo/Radio/PBFR) Therapy of Glioblastoma. *J. Mater. Chem. B* **2022**, *10*, 9794–9815. [CrossRef]
28. Costa, J.P.; Pinheiro, T.; Martins, M.S.; Carvalho, M.F.N.N.; Feliciano, J.R.; Leitão, J.H.; Silva, R.A.L.; Guerreiro, J.F.; Alves, L.M.C.; Custódio, I.; et al. Tuning the Biological Activity of Camphorimine Complexes through Metal Selection. *Antibiotics* **2022**, *11*, 1010. [CrossRef]
29. Hachem, H.; Le Gal, Y.; Jeannin, O.; Lorcy, D.; Scalese, G.; Pérez-Díaz, L.; Gambino, D.; Matos, A.P.; Marques, F. Metal (Au, Pt, Pd, Ni) Bis(Dithiolene) Complexes as Dual-Action Agents Combating Cancer and Trypanosomatid Infections. *J. Inorg. Biochem.* **2025**, *264*, 112788. [CrossRef]
30. Waks, A.G.; Winer, E.P. Breast Cancer Treatment. *JAMA* **2019**, *321*, 288. [CrossRef]
31. Agostinetto, E.; Gligorov, J.; Piccart, M. Systemic Therapy for Early-Stage Breast Cancer: Learning from the Past to Build the Future. *Nat. Rev. Clin. Oncol.* **2022**, *19*, 763–774. [CrossRef]
32. Tagliazucchi, M.; Peleg, O.; Kröger, M.; Rabin, Y.; Szleifer, I. Effect of Charge, Hydrophobicity, and Sequence of Nucleoporins on the Translocation of Model Particles through the Nuclear Pore Complex. *Proc. Natl. Acad. Sci. USA* **2013**, *110*, 3363–3368. [CrossRef]
33. García-Mendiola, T.; Bayon-Pizarro, V.; Zaulet, A.; Fuentes, I.; Pariente, F.; Teixidor, F.; Viñas, C.; Lorenzo, E. Metallacarboranes as Tunable Redox Potential Electrochemical Indicators for Screening of Gene Mutation. *Chem. Sci.* **2016**, *7*, 5786–5797. [CrossRef]
34. Froehlich, K.; Haeger, J.-D.; Heger, J.; Pastuschek, J.; Photini, S.M.; Yan, Y.; Lupp, A.; Pfarrer, C.; Mrowka, R.; Schleußner, E.; et al. Generation of Multicellular Breast Cancer Tumor Spheroids: Comparison of Different Protocols. *J. Mammary Gland Biol. Neoplasia* **2016**, *21*, 89–98. [CrossRef]
35. Souza, A.G.; Silva, I.B.B.; Campos-Fernandez, E.; Barcelos, L.S.; Souza, J.B.; Marangoni, K.; Goulart, L.R.; Alonso-Goulart, V. Comparative Assay of 2D and 3D Cell Culture Models: Proliferation, Gene Expression and Anticancer Drug Response. *Curr. Pharm. Des.* **2018**, *24*, 1689–1694. [CrossRef] [PubMed]
36. Theiner, S.; Schreiber-Brynzak, E.; Jakupec, M.A.; Galanski, M.S.; Koellensperger, G.; Keppler, B.K. LA-ICP-MS Imaging in Multicellular Tumor Spheroids—A Novel Tool in the Preclinical Development of Metal-Based Anticancer Drugs. *Metallomics* **2016**, *8*, 398–402. [CrossRef] [PubMed]
37. Grantab, R.H.; Tannock, I.F. Penetration of Anticancer Drugs through Tumour Tissue as a Function of Cellular Packing Density and Interstitial Fluid Pressure and Its Modification by Bortezomib. *BMC Cancer* **2012**, *12*, 214. [CrossRef]
38. Raitanen, J.; Barta, B.; Hacker, M.; Georg, D.; Balber, T.; Mitterhauser, M. Comparison of Radiation Response between 2D and 3D Cell Culture Models of Different Human Cancer Cell Lines. *Cells* **2023**, *12*, 360. [CrossRef]

39. Desouky, O.; Ding, N.; Zhou, G. Targeted and Non-Targeted Effects of Ionizing Radiation. *J. Radiat. Res. Appl. Sci.* **2015**, *8*, 247–254. [CrossRef]
40. Klein, S.; Sommer, A.; Distel, L.V.R.; Neuhuber, W.; Kryschi, C. Superparamagnetic Iron Oxide Nanoparticles as Radiosensitizer via Enhanced Reactive Oxygen Species Formation. *Biochem. Biophys. Res. Commun.* **2012**, *425*, 393–397. [CrossRef]
41. Rahmanian, N.; Hosseinimehr, S.J.; Khalaj, A. The Paradox Role of Caspase Cascade in Ionizing Radiation Therapy. *J. Biomed. Sci.* **2016**, *23*, 88. [CrossRef] [PubMed]
42. Jiao, Y.; Cao, F.; Liu, H. Radiation-Induced Cell Death and Its Mechanisms. *Health Phys.* **2022**, *123*, 376–386. [CrossRef]
43. Adjemian, S.; Oltean, T.; Martens, S.; Wiernicki, B.; Goossens, V.; Vanden Berghe, T.; Cappe, B.; Ladik, M.; Riquet, F.B.; Heyndrickx, L.; et al. Ionizing Radiation Results in a Mixture of Cellular Outcomes Including Mitotic Catastrophe, Senescence, Methuosis, and Iron-Dependent Cell Death. *Cell Death Dis.* **2020**, *11*, 1003. [CrossRef]
44. Boren, J.; Brindle, K.M. Apoptosis-Induced Mitochondrial Dysfunction Causes Cytoplasmic Lipid Droplet Formation. *Cell Death Differ.* **2012**, *19*, 1561–1570. [CrossRef] [PubMed]
45. McMahon, S.J.; Prise, K.M. A Mechanistic DNA Repair and Survival Model (Medras): Applications to Intrinsic Radiosensitivity, Relative Biological Effectiveness and Dose-Rate. *Front. Oncol.* **2021**, *11*, 689112. [CrossRef] [PubMed]
46. Di Maria, S.; Belchior, A.; Romanets, Y.; Paulo, A.; Vaz, P. Monte Carlo Dose Distribution Calculation at Nuclear Level for Auger-Emitting Radionuclide Energies. *Appl. Radiat. Isot.* **2018**, *135*, 72–77. [CrossRef]
47. Villagrasa, C.; Baiocco, G.; Chaoui, Z.-E.-A.; Dingfelder, M.; Incerti, S.; Kundrát, P.; Kyriakou, I.; Matsuya, Y.; Kai, T.; Parisi, A.; et al. Evaluation of the Uncertainty in Calculating Nanodosimetric Quantities Due to the Use of Different Interaction Cross Sections in Monte Carlo Track Structure Codes. *PLoS ONE* **2026**, *21*, e0340500. [CrossRef]
48. Perkins, S.T.; Cullen, D.E.; Seltzer, S.M. *Tables and Graphs of Electron-Interaction Cross Sections from 10 EV to 100 GeV Derived from the LLNL Evaluated Electron Data Library (EEDL), Z = 1–100*; University of California: Livermore, CA, USA, 1991.
49. Viñas, C.; Pedrajas, J.; Bertran, J.; Teixidor, F.; Kivekäs, R.; Sillanpää, R. Synthesis of Cobaltabis(Dicarbollyl) Complexes Incorporating Exocluster SR Substituents and the Improved Synthesis of [3,3′-Co(1-R-2-R′-1,2-$C_2B_9H_9)_2$]—Derivatives. *Inorg. Chem.* **1997**, *36*, 2482–2486. [CrossRef]
50. Hawthorne, M.F.; Andrews, T.D. Carborane Analogues of Cobalticinium Ion. *Chem. Commun.* **1965**, *19*, 443. [CrossRef]
51. Goorley, J.; James, M.; Booth, T.; Brown, F.; Bull, J.; Cox, L.; Durkee, J., Jr.; Elson, J.; Fensin, M.; Forster, R., III; et al. *Initial MCNP6 Release Overview—MCNP6 Version 1.0*; National Laboratory, New Mexico: Los Alamos, NM, USA, 2013; Volume 180.
52. Goddu, S.M.; Howell, R.W.; Rao, D. V Cellular Dosimetry: Absorbed Fractions for Monoenergetic Electron and Alpha Particle Sources and S-Values for Radionuclides Uniformly Distributed in Different Cell Compartments. *J. Nucl. Med.* **1994**, *35*, 303–316.
53. Borbinha, J.; Ferreira, P.; Costa, D.; Vaz, P.; Di Maria, S. Targeted Radionuclide Therapy Directed to the Tumor Phenotypes: A Dosimetric Approach Using MC Simulations. *Appl. Radiat. Isot.* **2023**, *192*, 110569. [CrossRef] [PubMed]
54. Cook, D.C. In-Situ Identification of Iron--Zinc Intermetallics in Galvannealed Steel Coatings and Iron Oxides on Exposed Steel. *Hyperfine Interact.* **1998**, *111*, 71–82. [CrossRef]
55. Gabbasov, R.; Polikarpov, M.; Safronov, V.; Sozontov, E.; Yurenya, A.; Panchenko, V. Monte Carlo Simulation of Dose Distribution in Water around 57Fe3O4 Magnetite Nanoparticle in the Nuclear Gamma Resonance Condition. *Hyperfine Interact.* **2016**, *237*, 34. [CrossRef]